EPD-iSCAT: Electrophoretic mass photometry

Matthew D. Kowal,[†] Teresa M. Seifried,[†] Carraugh C. Brouwer,[†] Hooman Tavakolizadeh,[†] Erik Olsén,[‡] and Edward Grant[*,†]

[†]*Department of Chemistry, University of British Columbia, Vancouver, BC V6T 1Z1 Canada*

[‡]*Michael Smith Laboratories, University of British Columbia, Vancouver, BC V6T 1Z4 Canada*

E-mail: edgrant@chem.ubc.ca

Abstract

Interferometric scattering microscopy (iSCAT) has rapidly developed as a quantitative tool for the label-free detection of single macromolecules and nanoparticles. In practice, this measurement records the interferometric scattering signal of individual nanoparticles in solution as they land and stick on a coverslip, exhibiting an intensity that varies linearly with particle volume, and an adsorption rate that reflects the solution-phase transport kinetics of the system. Together, such measurements provide a multidimensional gauge of particle size and concentration in solution over time. However, the landing kinetics of particles in solution also manifest a measurement frequency limitation imposed by the slow long-range mobility of particle diffusion to the measurement interface. Here we introduce a new technique that offers a novel means to overcome the inherent diffusion-controlled sampling limitation of spontaneous mass photometry. We term this methodology, electrophoretic deposition interferometric scattering microscopy (EPD-iSCAT). This approach uses a coverslip supporting a conductive thin film of indium tin oxide (ITO). Charging this ITO film to a potential

of around 1 V electrophoretically draws charged nanoparticles from solution and binds them in the focal plane of the microscope. Regulating this potential offers a direct means to control particle deposition. Thus, we find for a 0.1 nM solution of 50 nm polystyrene nanoparticles that the application of +1 V to an EPD-iSCAT coverslip assembly drives a electrophoetic deposition rate constant of 1.7 s^{-1} μm^{-2} nM^{-1}. Removal of the potential causes deposition to cease. This user control of EPD-iSCAT affords a means to apply single-molecule mass photometery to monitor long-term changes in solution owing to slow kinetic processes. In contrast with conventional coverslips chemically derivatized with charged thin films, EPD-iSCAT maintains a deposition rate that varies linearly with bulk concentration.

Introduction

Interferometric scattering (iSCAT) microscopy affords an effective label-free means to detect single nanoparticles in solution with exacting time, space and molecular mass resolution.[1–3] This methodology has emerged as a tool of rapidly growing importance owing to its high optical sensitivity, sufficient to precisely resolve particle mass on a scale of 10 kD or less[4] and spatially localize particle motion on a 10 nm length scale.[5] These features offer particular advantages for biophysical studies, tracking protein interactions, monitoring the formation of oligomeric states and aggregates, as well as resolving motion under conditions of confined diffusion in cell membranes and mimetics.[6–12]

The quantitative application of iSCAT relies on the linear variation of the interferometric contrast with the scattering amplitude of a nanoparticle, which, within a class of substances, depends directly on particle volume or mass. This relationship forms the basis of mass photometry (MP), which detects the light scattered by a single nanoparticle and quantifies it as a mass.[2,13] This conventionally occurs within the focal plane of an inverted microscope, set to the interface between the coverslip and a solution of analyte. Brownian motion spontaneously drives nanoparticles in solution to approach the coverslip. In a conventional iSCAT

experiment, such particles become immobilized upon collision by favorable interactions with a functionalized coverslip. This detection scheme provides high levels of optical sensitivity in part owing to the dynamic motion of particles, which are computationally separable from the static background reflection of the coverslip by ratiometric signal processing.[14]

Such an iSCAT mass photometric measurement occurs only when a nanoparticle migrates to the coverslip, collides, and binds. Thus, the solution phase particle dynamics strongly affect signal acquisition. The precise registry of particle size and location demands a fast and permanent immobilization of the colliding analyte onto the coverslip surface. This requires a careful match of the substrate and its surface chemistry to the properties of the analyte. Measurement success critically relies on a sufficient binding energy to the surface and the spontaneous migration of particles in solution.[15] The rate of solution-phase migration of the analyte to the coverslip often determines the sampling rate observed in a mass photometry measurement.

As conventionally implemented, iSCAT mass photometry relies on a coverslip substrate surface chemistry that is immutable over the duration of the measurement interval. This means that all deposition occurs spontaneously and the initiation of a measurement is strictly linked to the time of sample introduction. iSCAT microscopy offers a straightforward, real-time view of solution dynamics adjacent to the coverslip surface. However, for typical particle sizes, rapid deposition coupled with a diffusion-limited repopulation of this layer, limits the practical interval of measurement to no more than a minute or so, during which the experimental sampling rate falls by an order of magnitude or more.

We have studied this effect insofar as it determines the deposition rate of gold nanoparticles (AuNPs).[16] Observations of deposition rate as a function of time various nanomolar concentrations of 5, 10 and 15 nm AuNPs point to the strong, short-range attraction of negatively charged nanoparticles to a coverslip supporting a monolayer of positively charged functional groups, such as poly-D-lysine (PDL) at neutral pH. For example, the binding of 10 nm AuNPs from a 1 nM solution to a PDL coverslip depletes the adjacent nanoparticle

concentration, creating a solute concentration gradient that extends tens of microns into the solution and retards the rate of deposition to its diffusion-controlled limit in one minute or less.

Electrophoretic deposition interferometric scattering microscopy (EPD-iSCAT) replaces surface functional group binding with an electrostatic-potential-driven sampling methodology that enables direct user control of particle deposition for mass-resolved single-nanoparticle detection. Instead of an immutable, chemically functionalized coverslip, EPD-iSCAT uses the electrostatic field established by a potential applied between the indium tin oxide (ITO) thin film on the coverslip and a reference electrode to drive electrophoretic migration of nanoparticles in solution, ending with electrostatic binding to the coverslip surface. EPD-iSCAT offers a superior binding performance that can be reversibly modulated by varying the applied potential. Furthermore, this methodology allows a measurement to begin independent of the time of sample introduction, enabling binding and detection at periodic intervals.

Experiments with polystyrene nanoparticles demonstrate that such an electrostatic potential gradient can cycle periods of solute binding on and off for a wide range of particle sizes. Furthermore, we show that no depletion layer develops to affect the rate of deposition, which instead depends linearly on the concentration of solute in solution. The present work introduces a new measure of interferometric contrast based upon an image standard deviation metric, and shows that EPD-iSCAT signals correlate to the scattering power of a nanoparticle to a degree that depends on its mass or size in proportion to its diameter cubed. EPD-iSCAT unlocks a dimension of experimental control that was previously relinquished to the autonomous nature of spontaneous deposition. The direct control of sampling allows for iSCAT integration into a range of new technologies, particularly those involving the procession of slow time-dependent events, which commonly occur in biological systems, nanoparticle synthesis, and automated microscale assays.

Results

Detection of individual nanoparticle adsorption during electrophoretic deposition

An iSCAT microscope records the deposition of individual nanoparticles as diffraction limited point spread functions. Figure 1 shows 25, 50, 100, and 200 nm polystyrene nanoparticles (PSNPs) appearing in three different visual representations. The bottom row shows TEM micrographs representative of each sample. For each particle size, a Hough circle transform applied to a set of TEM images generates a normal particle size distribution histogram. A Gaussian curve fit to the data approximates a mean diameter and standard deviation as listed below in Table 1. Note that sample uniformity and contrast decrease with decreasing particle size and increasing resolution. TEM images of 25 nm and 50 nm particles contain many instances of low-contrast debris.

The middle row of Figure 1 shows still frames captured from an EPD-iSCAT ratiometric video during the deposition of PSNPs from solution onto an ITO coated glass coverslip. When an iSCAT microscope is focused on the interface between a coverslip and solution, depositing nanoparticles are immobilized and imaged as a tightly focused point spread function. However, the small change in brightness associated with this event is nearly invisible when viewed in raw video (Figure S2). Accurate particle detection and measurement requires signal processing to isolate the weak scattering signal from the overwhelmingly bright background. Ratiometric signal processing uses a stream of sequential images to amplify temporal changes in image intensity while simultaneously normalizing the unchanging background. This approach augments the iSCAT video signal in such a way that even small changes in image intensity appear as high contrast changes in brightness sitting atop a grey background. Since ratiometric signal processing is a pixel-wise convolution in time, each deposition event materializes as a stationary point spread function that increases in contrast to reach a maximum when the ratiometric buffer is half full, followed by a symmetric decrease

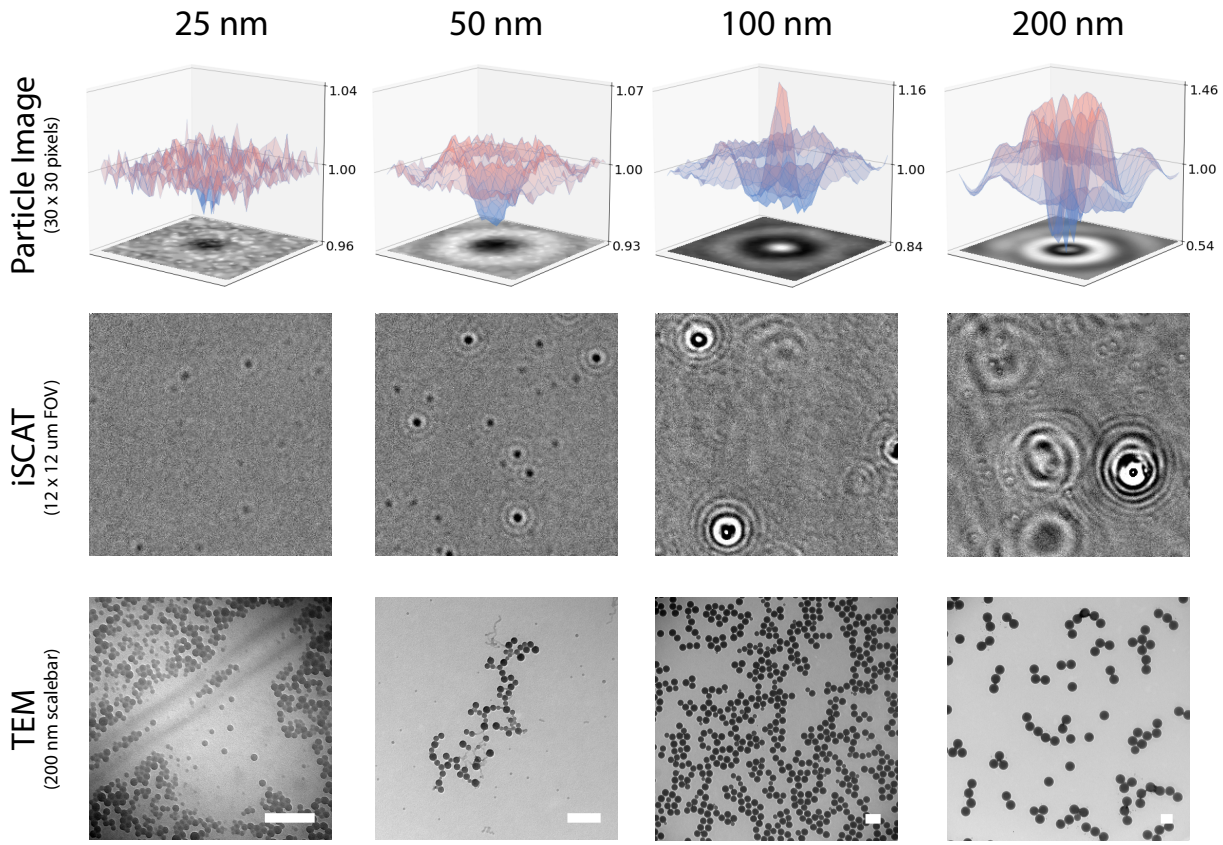

Figure 1: (Top) Detected point spread functions associated with single 25, 50, 100, 200 nm polystyrene nanoparticle (PSNP) deposition events on a charged ITO coated coverslip. Individual particle images min/max scaled following the z-axis scale. (Middle) PSNP depositions revealed by ratiometric image processing of an iSCAT video for each particle size (image scaling black and white clipped to 0.97 and 1.03 respectively, field-of-view: 12 x 12 μm). (Bottom) Transmission electron micrography (TEM) images of the same PSNPs (scalebar: 200 nm) show many highly spherical particles.

in contrast as the particle image fills the ratiometric buffer, and the signal fades into the grey background.

Particles are detected and localized by a YOLO v8 object-detection model[17] trained on local experimental data. The top row of Figure 1 shows 30 x 30 pixel images of particle depositions captured during frames of maximum contrast. A surface plot hovering above each image illustrates the amplitude of the point-spread function as it increases with particle size. Here, surface plots display mean-centered 16-bit floating point pixel counts as produced by the ratiometric signal processor. Below, the particle images display the same image

min/max scaled to an 8-bit bitmap, illustrating a signal-to-noise ratio highly dependent on PSNP diameter. For 100 and 200 nm PSNPs, high intensity central amplitudes are observed. Thousands of detected particle contrast measurements produce a distribution of particle scattering intensities for each PSNP diameter with a distribution describing the sample polydispersity. These values are listed below in Table 1.

Kinetics of EPD-iSCAT electrophoretic nanoparticle deposition

In operation, an iSCAT microscope counts single-particle deposition events over time. Figure 2A (grey line) plots the diffusion-controlled deposition of a 0.05 nM solution of 50 nm polystyrene nanoparticles adsorbing onto a PDL coated coverslip. Particles immediately adsorb onto the substrate with a high initial rate of approximately 8 particles per second followed by a steady decline with square root dependence in time as expected for diffusion-limited deposition. In contrast, electrophoretic deposition of PSNPs with EPD-iSCAT (blue line) exhibits a strong dependence on the potential applied to the device (orange line). We observe no landings during the initial 30 s when the potential is zero. Upon the application of a +1 V potential, the rate of deposition quickly increases to a steady state for the duration of the applied potential. Deposition quickly ceases when the potential is removed after 90 s of observation.

As shown in Figure 2B the application of a square wave potential modulates deposition from a 0.05 nM solution of 50 nm PSNPs. Here, we see a very low rate of deposition during the initial 25 s of the experiment when the applied potential is zero. Then, the first application of a +1 V square wave pulse to the ITO coverslip begins an induction period of during which deposition in the region of interest rises to a rate of 14 particles per second, which remains constant until the potential is removed. Deposition ceases in the absence of applied potential and resumes promptly over time when we apply a sequence of square-wave pulses of +1 V. This cyclic potential-induced response continues with no change in rate for at least several minutes (Figure 2C). Remarkably, very little deposition occurs during intervals

of zero potential.

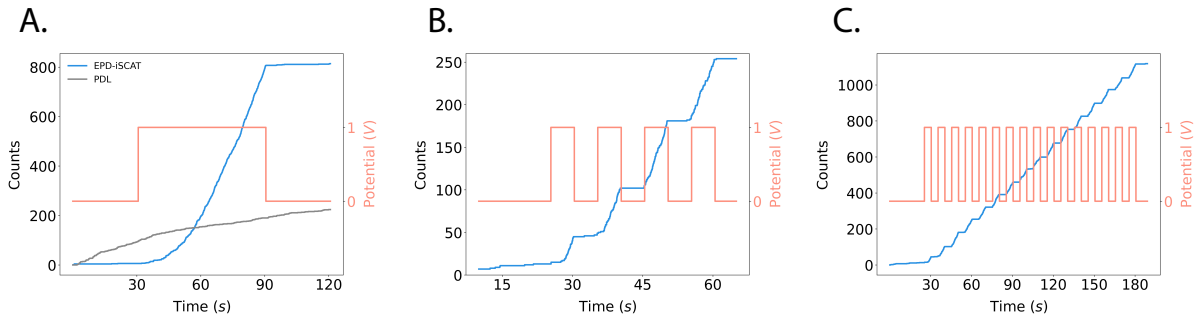

Figure 2: (A) Deposition of 50 nm PSNPs from a 0.05 nM suspension on an ITO coated coverslip (blue line) of an EPD-iSCAT experiment, under a modulated +1 V potential and a poly-D-lysine coated coverslip (grey line) in absence of an external voltage source. (B, C) Deposition of 50 nm PSNPs from a 0.05 nM suspension onto the EPD-iSCAT device during the application of a +1 V, 0.1 Hz square wave pulse train for (B) 40 s and (C) 3 min.

The rate of electrophoretic deposition varies with particle concentration. Figures 3A and B chart the average number of 50 nm PSNPs deposited as a function of time from solutions with particle concentrations of 0.005, 0.025, 0.05, 0.15 and 0.25 nM, upon applying a 60 s square wave pulse within an observation window of two minutes. Here we plot the average of the deposition count as a function of time, observed in at least four experiments with confidence bands spanning one standard deviation. Notably, the rate of deposition increases linearly with nanoparticle concentration and the experiment detects very few particle landings in the absence of an applied potential. Note here as in Figure 2 that the first application of potential produces a relatively slow rise in deposition frequency. Thereafter, deposition proceeds at a constant rate, regulated by the concentration in solution. Least-squares fits to the deposition rates in Figure 3 over the measurement interval from 60 to 90 s for each concentration combine to yield a rate constant of 3.4 s^{-1} μm^{-2} nM^{-1} for the electrophoretic deposition of 50 nm PSNPs onto a 10.6 x 10.6 µm region of interest with a +1 V applied potential.

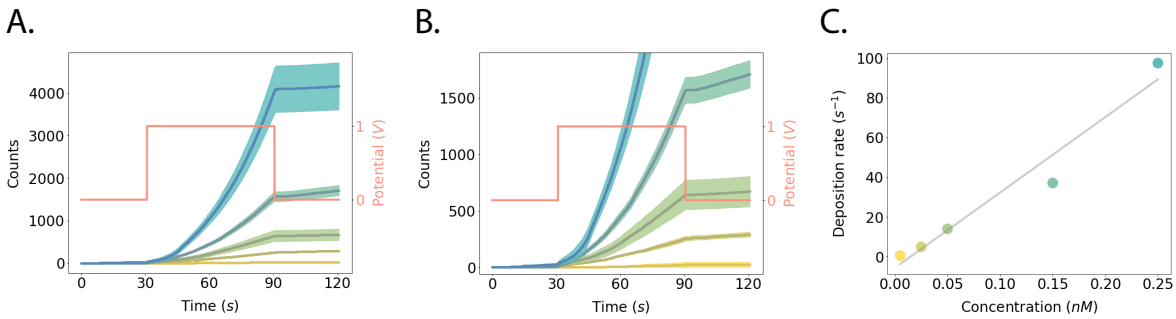

Figure 3: (A, B) Average particle deposition counts of 50 nm PSNPs at different concentrations (0.005, 0.025, 0.05, 0.15, 0.25 nM - yellow to green) as a function of time and applied potential (orange line). Confidence bands spanning one standard deviation surround the average deposition count. (C) Average deposition rate of 50 nm PSNPs as a function of PSNP concentration.

EPD-iSCAT mass photometry of nanoparticles

Table 1 compares the average iSCAT contrast measured for solutions of nominal 25, 50, 100 and 200 nm PSNPs with particle diameters determined from TEM micrographs. The measurements exhibit normal distributions and a Gaussian fit to the data provides a central value and size distribution. Here, the standard deviation is a measure of the polydispersity of the sample, rather than a measurement error. iSCAT scattering intensity is recognized to scale as a function of the particle diameter raised to the power of three. Consequently, the cube root of iSCAT contrast establishes a linear relationship correlated to the measured TEM particle diameters listed in Table 1.

Table 1: Distribution of EPD-iSCAT contrast$^{1/3}$ measured for PSNPs of nominal diameter, 25, 50, 100 and 200 nm, compared with physical particle dimensions measured by TEM.

Nominal	EPD-iSCAT			TEM		
Diameter	Measurements	(Contrast)$^{1/3}$	σ	Measurements	Diameter	σ
25	9961	0.171	0.007	1658	22	6
50	14240	0.212	0.023	2348	35	9
100	4628	0.381	0.027	3817	96	5
200	699	0.606	0.024	652	166	3

Figure 4 shows histograms of measured TEM diameter (right) and cube root iSCAT contrast (top). A kernel density estimation generates a central value and standard deviation

to the normal distributions. Figure 4 (center) plots mean TEM diameter against mean iSCAT contrast for each PSNP size. Error bars representing one standard deviation reflect the polydispersity of measurements, evident in the width of each histogram. A linear least-squares regression produces a calibration curve for iSCAT contrast relative to particle size with $r^2 = 0.998$. For PSNPs, the diameter (D) dependent calibration constants of cube root iSCAT contrast $C_{ps}^{1/3}$ for the EPD-iSCAT device is calculated to be $C_{ps}^{1/3} = 3.02 \times 10^{-3} nm^{-1}$ with an RMS error of 1.98 nm

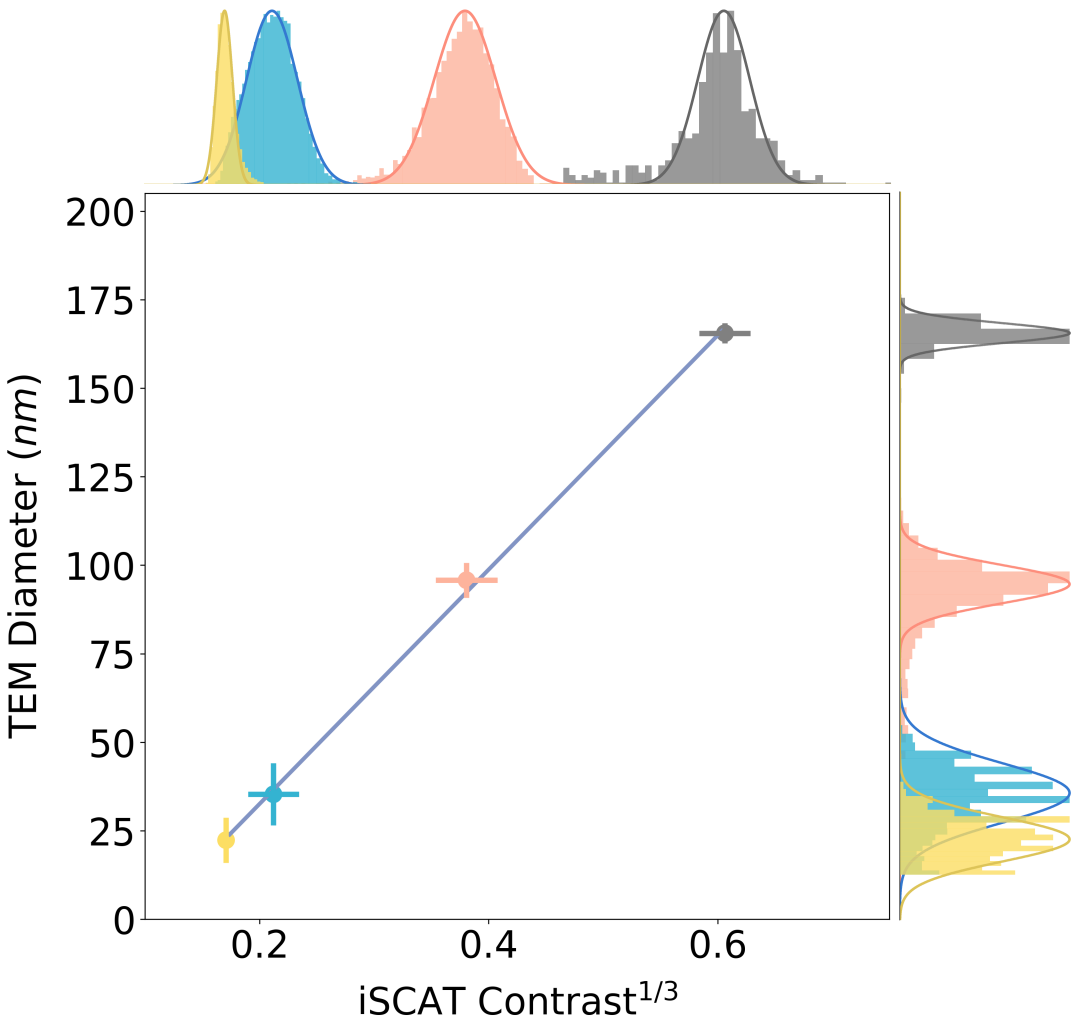

Figure 4: Calibration plot relating the cube root iSCAT contrast to TEM measured particle diameter for 25, 50, 100 and 200 nm PSNPs (represented by yellow, blue, orange, and grey respectively). Error bars correspond to the standard deviation of each Gaussian fit. The top displays the cube root contrast distribution for PSNPs accumulated from EPD-iSCAT measurements and the right the physical diameter dimensions measured by TEM.

Discussion

Ratiometric signal processing facilitates internal validity

The deposition of a single nanoparticle produces an image composed of the interference of its scattered light with that reflected as a plane wave from the interface of the coverslip with the solution. Ratiometric imaging reports the intensity of that interference as a quantity proportional to a contrast defined by the standard deviation of the image in a shot-noise-limited background. For particles much smaller than a wavelength of light, isolating this interference term yields a metric which scales linearly with the mass or volume. Deviations from linearity have been measured for large particles approaching the diffraction-limit.[18] The degree to which measurements follow this linear scaling can depend on the specific optical configuration, the material properties of the analyte and the metric used to describe interferometric contrast. The treatment of ratiometric image information thus plays a critical role in determining the accuracy and precision of a mass photometric measurement.

An initial step in the digital processing of raw data amplifies the single-shot image contrast by accumulating a ratiometric signal over time. Ratiometric processing of images acquired at a frame rate of 200 s^{-1} with typical signal and background buffers of 20 frames allows for direct, real-time observation of particles 20x smaller than the incident wavelength, greatly facilitating a computer vision approach to particle detection. Although landings of nanoparticles larger than 100 nm do not require ratiometric processing to observe, a measurement strategy that approaches all particle sizes of interest ratiometrically offers two practical advantages. With all ratiometric video streams mean-centered to one, a global measurement readily acquires an element of self-consistency by normalizing the absolute image intensity variations between samples. Secondly, the acquisition of signal in frame buffers affords an opportunity to throttle background noise by varying the number of frames in the buffer. This conforms with noise reduction by altering the number of averaged frames.

Single particle images appear as point spread functions with a contrast that grows linearly

in time until the signal fills the leading ratiometric buffer. Then, as the second ratiometric buffer begins to fill, the signal fades steadily into the background with each subsequent frame. This yields a time series of contrast measurements for each particle. We take full advantage of ratiometric averaging by recording the iSCAT signal at the point of maximum contrast.

Relation between particle scattering amplitude and the interference signal: Standard deviation as a measure of contrast

The smallest detectable particles form faint dark-centered spots with a contrast that barely rises above the background noise. With little amplitude apportioned to coaxial rings, a simple two-dimensional Gaussian function serves well to describe these point-spread functions.[1,2,13,19,20] The interferometric contrast scales with the area of the Gaussian, or its amplitude, given its constant diffraction-limited diameter. This simple representation holds for particle diameters much smaller than the laser wavelength. Particles larger than 50 nm produce a more complex interferometric scattering pattern, with a substantial fraction of the contrast partitioned to intense concentric rings. For a sample diameter larger than 100 nm, the light scattered from a PSNP forms an image that exhibits a bright center, which is poorly represented by a simple two-dimensional Gaussian function. This transition from destructive to constructive interference arises from several competing factors.

According to conventional iSCAT theory, signal intensity measured at the detector, I_{det} is defined by $I_{det} = |E_i|^2[r^2 + s^2 + 2rs\cos(\delta\phi)]$ where E_i is the incident electric field, r is the proportion of light reflecting from the coverslip and s is the proportion of light scattering from the object and $\delta\phi$ is the phase difference between these fields. For homogeneous spheres with diameters less than a few tens of nanometers, we can assume that the pure scattering term s^2 contributes negligibly to the signal,[21] that the background, r, remains constant, and when the small particle is bound to and located at the reference plane, the phase difference, $\delta\phi$ remains constant. These assumptions lead to a detected optical field that is modulated only by the scattering optical field, which is proportional to particle volume.[22] The utility of

mass photometry relies on this important relationship. However, as particle size increases, non-negligible scattering, s^2, as well as interference from different scattering sub-units within the particle cause a deviation from linearity. Additionally, phase shifts along the scattering volume of larger particles adds further complexity to the scattering model and a constant $\delta\phi$ is no longer a good assumption. Moreover, defocusing of the image further affects the relative phase offset via the Gouy phase.[23,24]

We sidestep these complexities by taking a statistical approach to the determination of contrast. Ratiometric signal processing yields a normalized amplitude distribution with mean-centering at one. The dynamically sampled interference signal produced by the landing of a particle causes the signal to depart from unity and the magnitude of this departure, measured by the standard deviation of the pixels in the region of interest, varies in direct proportion to the interferometric contrast. As a practical matter, calculating the standard deviation is computationally much more efficient than a two-dimensional Gaussian regression, even in the small-particle case of a Gaussian point-spread function. Additionally, standard deviation requires no prior knowledge of the imaging system, which would be required if the signal was fitted to comprehensive optical simulations. One might expect to find non-linear signal-size scaling for the largest particle sizes investigated here. But, standard deviation sampling appears to produce a measure of contrast that scales linearly with volume up to that of particles as large as a TEM-measured average of 166 nm. We have performed Mie scattering simulations that replicate this behaviour (see Supporting Information). Simulations suggest that this trend holds for particle diameters below 190 nm, although system specific differences including the refractive index of the particle and medium and the reflectivity of the coverslip and particle reflector[25,26] may alter this range.

The electrostatics of EPD-iSCAT and the kinetics of particle binding

An iSCAT microscope records mass-resolved deposition events with a frequency that reflects the concentration of particles in the solution immediately adjacent to the coverslip. If the

rate of binding exceeds the rate at which particles of any particular mass diffuse to refill this volume, the landing frequency of those particles will fall to measure the net rate at which diffusion from solution fills the depletion layer.[16] We see an example of this effect in the grey curve in Figure 2A showing the rate of PSNP deposition on a PDL coated coverslip decays with a square root of time dependence, indicating a characteristic diffusion limited process.

By contrast, we detect few if any particle landings at the start of an EPD-iSCAT measurement when the ITO potential is set to 0 V. At a chosen time later, Figure 2 shows that the application of a +1 V potential initiates deposition, which quickly rises to a constant rate that persists until the potential is reduced to zero. Figure 3 clearly establishes that the kinetics of deposition depend directly on the concentration of particles in the bulk solution. A charged ITO surface acts much like PDL to deplete the immediately adjacent nanoparticles. Evidence for this appears in the initial rate of deposition on PDL compared with that on an ITO when charged to +1 V. However, in the case of EPD-iSCAT, electrophoretic migration, driven by the potential field between the coverslip and the reference electrode, replenishes coverslip-adjacent nanoparticles depleted by deposition.

Under steady-state conditions, the Smoluchowski equation of electrophoretic mobility describes the velocity, v, of a charged particle in solution moving in an electric field, E:

$$v = E\epsilon_r\epsilon_0\zeta/\eta \tag{1}$$

ϵ_r is the dielectric constant of the solution, ϵ_0 is the permittivity of free space, ζ is the zeta potential of the nanoparticle, and η is the dynamic viscosity of the solution. At constant voltage, a constant electric field produces a steady state velocity. Thus, the EPD-iSCAT rate of deposition reflects the constant velocity of steady-state electrophoresis, which produces a flux of particles that is directly proportional to their concentration. Moreover, the measured rate of nanoparticle deposition provides a means of measuring the zeta potential of an analyte.

EPD electrode voltage range

Electrophoretic deposition produces reliable, single particle landings for applied potentials held to near +1 V. ITO voltages outside of this range give rise to varying effects on the deposition behavior. At neutral pH, ITO has a positive zeta potential.[27] Thus, under certain conditions of particle mass and concentration, spontaneous deposition of negatively charged particles can occur in the absence of an applied potential. Applying a negative charge to the ITO substrate can repel negatively charged particles and prevent spontaneous binding. When the ITO substrate is charged below a certain threshold voltage, typically +0.8 V, particles appear to approach and diffuse along the coverslip surface for a several seconds before leaving the region of interest. This effect signals a substrate surface charge that is too weak to overcome Brownian motion and the colloidal stability of the nanoparticle in solution. The time varying scattering intensity from a single particle diffusing along a coverslip is not easily modelled. However this effect might support a nanoparticle tracking analysis strategy that indirectly finds the mass of a particle by measuring its 2D diffusion coefficient[18,28] from high frame rate video feed.

We also find signs of a high voltage limit. After several minutes of exposure to high laser intensity and applied potentials above +1.2 V the refractive index gradient in the region of interest exhibits fluctuations, even when no analyte is present. These fluctuations manifest as sub-wavelength sized enduring changes in contrast, imaged ratiometrically as transient point spread functions. These images appear sharpest with a focus set several microns above the coverslip-solution interface. In other respects this signal is indistinguishable from the deposition of small nanoparticles. Fortunately, these artifacts appear only at high laser power (>200 mW) and high voltage (>+1.2 V), making them easily avoidable. We propose that these artifacts may be caused by bubble formation during the electrolysis of water. Continued exposure to high laser powers in combination with high voltage causes the ITO

film to degrade to a brown film with very poor optical qualities,[29] presumably from the reduction of nano-sized crystallites of indium oxide and tin oxide.

Summary advantages of EPD-iSCAT

Conventional iSCAT mass photometry affords a powerful tool for detecting and tracking nanoparticles in a focal plane set to the interface of the coverslip and the sample. But, sample-dependent electrostatic and kinetic phenomena present limitations. Implementation on a coverslip that is chemically functionalized to bind particles presents conditions under which spontaneous surface binding begins immediately upon introduction of the sample. Thereafter, the experimentally observed sampling rate rapidly becomes limited by the rate of diffusion of analytes in solution. This serves effectively to place a window on the time interval of optimal measurement.

EPD-iSCAT solves this problem while unlocking new dimensions of experimental control. The active application of an electrostatic field between the ITO coverslip and the reference electrode initiates a flux of particle deposition events. This determines when an interval of measurement begins and ends. Such intervals of user-controlled deposition offer enormous advantages, such as enabling discerning, extended single-molecule probes of protein-protein oligomerization and aggregation reactions, nanoparticle self-assembly and crystal growth. This feature also fits well with lab-on-a-chip and microfluidics applications that often require long intervals of time between sample introduction and measurement.

The element of electrophoresis gives EPD-iSCAT a further advantage. The transport of charged analyte to the ITO surface overcomes the rapid loss of surface-adjacent particles that occurs in deposition from a stagnant sample, providing instead a constant flux of analyte that depends linearly on its concentration in the bulk. This utility provides rapid nanoparticle solution characterization for determining the efficacy of newly developing chemical processes[30] while offering a reliable single-molecule window on long-time kinetic rate processes in complex solutions. Future work could well combine electrophoretic separation with EPD-

iSCAT mass photometric detection. In a single device, conventional electrophoresis in one dimension could separate macromolecule and/or nanoparticle analytes according to their electrophoretic mobility for detection by a transverse stage of EPD-iSCAT.

In another hybrid approach, an EPD-iSCAT optical assessment could add deeper meaning to nanoelectrochemical signals produced by the deposition of nanoparticles on electrode surfaces,[31–34] taking further advantage of iSCAT as a surface chemistry technique. Work up to now has used darkfield microscopy which lacks the sensitivity and mass specificity of iSCAT. The incorporation of high precision potentiostats and chronoamperometry able to measure the tiny changes in current on an electrode associated with single nanoparticle electrophoretic deposition events would add a new dimension to simultaneously acquired EPD-iSCAT mass photometry information.

Methods

Sample preparation

Monodisperse polystyrene nanoparticle material standards were supplied by several manufacturers. PSNPs of the sizes 50, 100, 200 nm were purchased from Polysciences (50 nm Cat: 08691-10 lot: A798553), (100 nm, Cat: 00876-15, Lot: A808303), (200 nm, Cat: 07304-15, A808636) and 25 nm PSNPs were purchased from CD bioparticles (25 nm, Cat: DMP-L001, Lot: JQM1918). All nanoplastic samples contain a small amount of surfactant. Material standards were diluted with deionized water to produce a series of concentrations from 1.0 nM to 0.01 nM.

Electrophoretic device fabrication and use

An ITO coated glass coverslip provided by SPI Supplies (1.5 thickness, 70 - 100 70 Ω/sq, Cat; 6486B-AB) serves as an imaging plane for the optical system, an electrode which enables electrophoresis, and a positively charged surface for electrostatic binding of negatively

charged nanoparticles. The ITO coverslip is mounted to the sample holder and secured on either side by 1/8 inch wide Kapton tape. Copper tape connected to the coverslip busbar acts as an electrical contact for the power supply. The counter electrode (0.5 mm graphite rod) is suspended 3 mm above the ITO by a solid armature. The sampling medium (10 μL deionized water) is placed between and contacts both electrodes. A National Instruments PCIe-6321 card supplies a voltage to the device through a National Instruments SCB-68A DAQ. During a typical experiment, 10 μL of a nanoparticle solution is micro- pipetted into 10 μL of a sampling medium (deionized water). Immediately after the sample is introduced, solution turbulence and concentration gradients influence local particle kinetics, so we allow one minute for the dispersion to homogenize before data collection begins.

iSCAT optical system

A custom sample holder machined from 1.6 mm thick steel is focused with a low profile, through aperture, piezo controlled Z-stage (PI P-736-Zr2) mounted to a through-aperture XY stage (PI M-545.2MO). An illustration of the optical path is shown in Figure 5. Highly polarized, monochromatic light from a 532 nm solid state diode laser (Laser Quantum GEM 532 nm Diode-Pumped Solid State Laser) running at 150 mW illuminates the sample. The beam is guided into a diverging rectangular path by acousto-optic beam deflectors (AOBD, Gooch & Housego Model R72003) driven by voltage control oscillators (Gooch & Housego MLV050-90-2AC-A1) and modulated by a function generator (Tektronix AFG1062). Oscillating frequencies of 78 kHz and 80 kHz for the two AOBD crystals produce an evenly illuminated rectangle for exposures over 400 μs. A 4f system of 400mm lenses (L1 and L2) focuses the rectangular image to a point on the back of a high magnification oil-immersion objective (Olympus 60x PlanApo N, 1.42 NA), passing through a polarized beam splitting cube. The objective projects the rectangular beam path onto the water / coverslip interface, where the first significant change in refractive index occurs. Focusing on the interface produces a reference background image with a planar wavefront. A scattering object, in

focus at the water / coverslip interface during a binding event, produces a spherical wavefront which is refracted differently than the planar reference image.

A quarter waveplate placed between the PBS cube and the objective ensures that the polarization of the returning light is rotated by 90°, directing the image to the detection path via the PBS cube. On the detection path, a 400mm lens (L3) focuses an image onto the image plane of a 4f optical system consisting of 2x 400mm lenses (L4 and L5). The 4f optical system focuses the planar reference wave front to a point at the Fourier plane to be attenuated by a 2 mm diameter partial reflector, fabricated by depositing 100 nm of gold to the center of a 1-inch diameter NBK7 glass window. Conversely, the scattering object's spherical wavefront is collimated at this point and passes by the partial reflector with relatively little change to the signal intensity. The last lens (L5) of the 4f system projects the final image onto the camera sensor (Point Grey Grasshopper GS3-U3-51S5M).

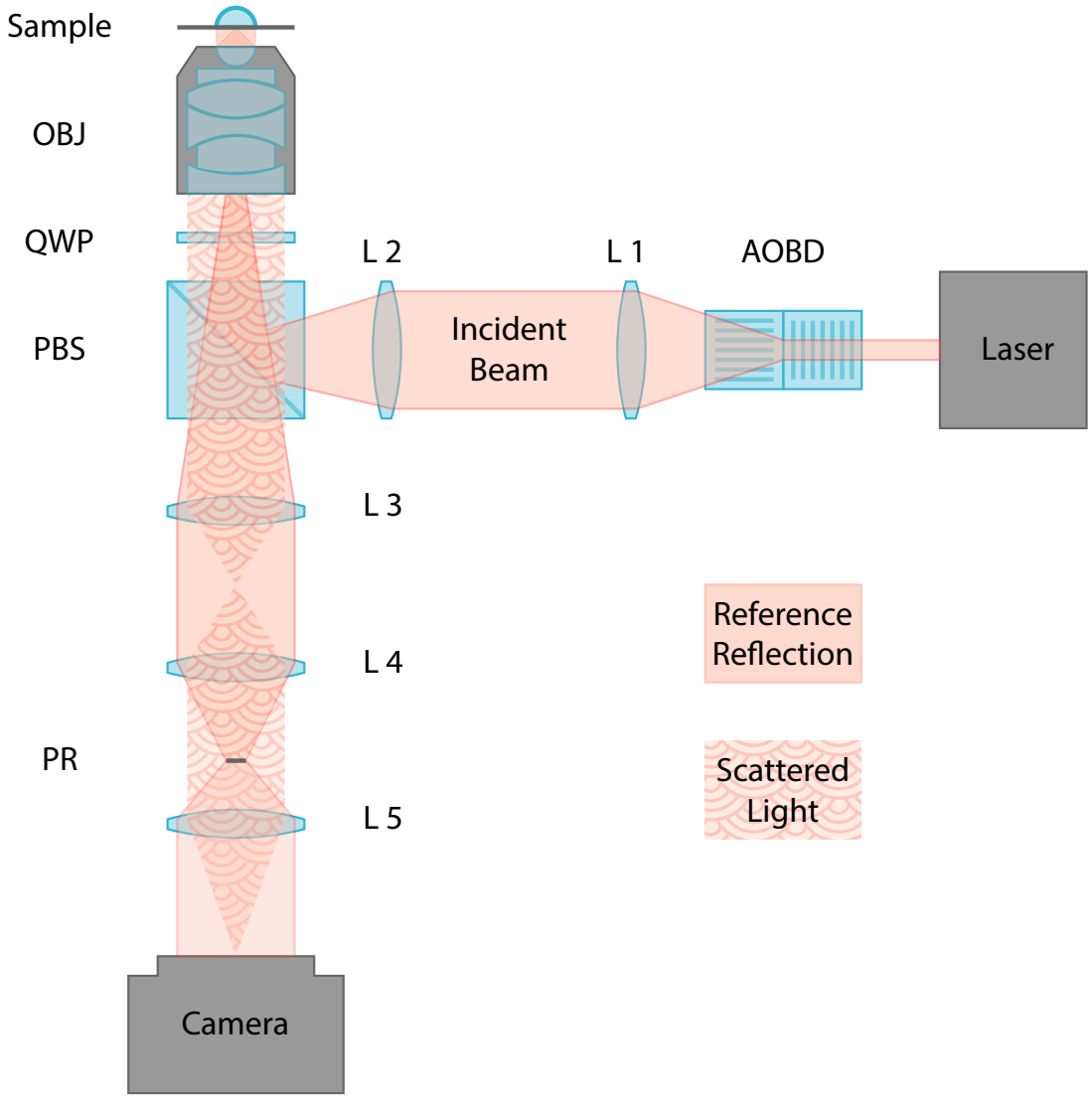

Figure 5: Schematic diagram of the iSCAT optical system. Components include 532 nm laser, acousto-optic beam deflector (AOBD), 4f optical systems (L1, L2, L4, L5), polarized beam splitter (PBS), quarter-wave plate (QWP), objective (OBJ), sample stage (Sample), image forming lens (L3), partial reflector (PR) and camera.

Data Processing

Data Acquistition and User Interface

A purpose-built graphical user interface, written in LabView, reads a stream of camera data while controlling laser power, AOBD output, Z-Stage focusing, and electrophoretic potential and provides a platform for user input and file management. The interface displays real-time

8-bit video captured from a 5 megapixel 2/3" Sony IMX250 monochrome CMOS sensor at 200 frames per second. A 12 x 12 μm field of view projects an image into 3.3 x 3.3 mm portion of the sensor covering 512 x 512 pixels. A single 3.45 x 3.45 μm pixel saturation capacity of 10,208 e^- provides a total saturation capacity of $2.67 \times 10^9\, e^-$ for all 262,144 pixels per frame. In-camera 2 x 2 pixel binning reduces the frame resolution to 256 x 256 pixels for a final pixel resolution 47 nm/pixel. Frames are exported to a binary file as a series of uncompressed bitmaps.

Video signal processing

A custom video signal processing routine written in Python converts raw 8-bit video into a ratiometric video with amplified luminescent sensitivity gained by the reduction in temporal resolution. The complete signal processing algorithm and peripheral software are available on Github (https://github.com/MatthewKowal/iscat-yolo). The construction of a ratiometric algorithm is described herein. Summarily, the ratiometric algorithm is a frame-by-frame process which generates each ratiometric video frame (f_{ratio}) from the quotient of two averaged sequences of video frames.

$$f_{ratio} = \frac{f_1 + f_2 + f_3 + ... + f_b}{f_{b+1} + f_{b+2} + f_{b+3} + ... + f_{2b}} \tag{2}$$

Each sequence of frames is constructed with a first-in-first-out (FIFO) buffer of length b. Recall that a FIFO buffer is a type of fixed-length queue where new items are added to one end of the queue and old items are dequeued from the opposite end. Video frames are treated similarly to people in a line such that the first frame to added to the queue is the first frame to be removed, however ratiometric signal processing requires two sequential queues. At the start of the video the first $2b$ number of frames fill both queues. New video frames are fed into the first buffer while overflowing frames are simultaneously moved to the second buffer and the oldest frames are dequeued and discarded. Generating a ratiometric image involves pixel-wise averaging of the entirety of each FIFO buffer, which produces two

images with reduced noise and decreased temporal resolution. The quotient of these images forms the ratiometric frame. The algorithm continues in a steady state condition, generating a new ratiometric image for every new raw frame throughout the length of the raw video.

In the absence of any inhomogeneous scattering objects the ratiometric video is composed of background of noise centered at unity. Upon particle deposition, a circular diffraction pattern is observed to fade in and out in intensity. The intensity of the signal increases linearly to reach a maximum contrast representing the maximum scattering amplitude of the depositing particle. The contrast subsequently fades to unity as the immobilized particle becomes part of the unchanging background. The number of frames required for the new particle signal to reach maximum contrast is equal to b, the length of the first ratiometric buffer. At this point, the numerator in the ratiometric quotient (*i.e.* the pixel-wise average of the first buffer) is maximally different than the denominator (the pixel-wise average of the second buffer) and the contrast reaches a peak. Measured contrast fades to unity over the same length of b frames as the second image buffer is filled with new, static, unchanging video frames and the denominator becomes equal to the numerator.

Particle detection

Particle detection is performed on the ratiometric video using YOLO v8 object detection framework.[17] A model is trained on a custom database of ratiometric images using 10 epochs and a batch size of 64. The model detects and localizes point spread functions on the screen in near real-time (Fig S2). The database contains over 1800+ images of particle landings and blank background images from iSCAT experiments. The image database was annotated using Roboflow online dataset management tool[35] and exported in the YOLO v8 format. The particle image dataset is open source and freely available.[36]

iSCAT contrast measurement

For each particle deposition in an experiment a 30 x 30 pixel image of the point spread function is recorded for each frame the particle is detected in. The sequence of frames forms a video approximately equal in length to the ratiometric buffer. The standard deviation is calculated for each video frame and the largest value is used as the maximum contrast for that particle.

TEM measurements

PSNP diameters are measured by TEM image analysis. Nanoparticle samples were prepared for imaging by drop-casting the samples into glow-discharged copper grids (200 mesh, Formvar coated from Ted Pella) and allowing them to dry on the grid for at least 24 h before imaging. A FEI Tecnai Spirit 120kV TEM operated at 80kV was used to collect nanoparticle micrographs at a magnification between 23,000x-68,000x, corresponding to 1.4 - 4.0 nm/pixel resolution. A custom Python script using a Hough Circle Transform automates the image analysis of the TEM micrographs, resulting in a distribution of diameter measurements. Over 8,000 particle instances were measured in total and no sample had less than 600 instances measured.

Acknowledgement

We gratefully acknowledge support of a Discovery Grant from The Natural Sciences and Engineering Research Council of Canada (RGPIN-2019-04242) and a grant from the New Frontiers in Research Fund (NFRFE-2020-01301) TEM services were provided by UBC Bioimaging Facility (RRID: SCR 021304). We thank Daniele Reda for assistance with setting up YOLO v8 and Luke Melo for technical support regarding the iSCAT optical system.

Supporting Information Available

Supporting information is available free of charge.

- EPD-iSCAT device construction, iSCAT image processing and particle detection example, Concentration measurement limits of detection, Mass photometry calibration limit of detection, Extending the lower limit of detection for mass photometry, Lower limit measurement variation between TEM and iSCAT, Upper limit measurement variation between TEM and iSCAT, Origin of nanoparticle charge, Particle-surface interactions, EPD electrode voltage threshold

- Movie S1: EPD-iSCAT voltage controlled deposition of 50 nm polystyrene nanoparticles. Field of view 12 x 12 µm, tick marks at every 1 s of experiment time.

References

(1) Ortega Arroyo, J.; Andrecka, J.; Spillane, K. M.; Billington, N.; Takagi, Y.; Sellers, J. R.; Kukura, P. Label-Free, All-Optical Detection, Imaging, and Tracking of a Single Protein. *Nano Letters* **2014**, *14*, 2065–2070, Publisher: American Chemical Society.

(2) Piliarik, M.; Sandoghdar, V. Direct optical sensing of single unlabelled proteins and super-resolution imaging of their binding sites. *Nature Communications* **2014**, *5*, 4495, Number: 1 Publisher: Nature Publishing Group.

(3) Young, G.; Kukura, P. Interferometric Scattering Microscopy. *Annual Review of Physical Chemistry* **2019**, *70*, 301–322.

(4) Dahmardeh, M.; Mirzaalian Dastjerdi, H.; Mazal, H.; Köstler, H.; Sandoghdar, V. Self-supervised machine learning pushes the sensitivity limit in label-free detection of single

proteins below 10 kDa. *Nature Methods* **2023**, *20*, 442–447, Number: 3 Publisher: Nature Publishing Group.

(5) Andrecka, J.; Ortega Arroyo, J.; Takagi, Y.; de Wit, G.; Fineberg, A.; MacKinnon, L.; Young, G.; Sellers, J. R.; Kukura, P. Structural dynamics of myosin 5 during processive motion revealed by interferometric scattering microscopy. *eLife* **2015**, *4*, e05413, Publisher: eLife Sciences Publications, Ltd.

(6) Asor, R.; Kukura, P. Characterising biomolecular interactions and dynamics with mass photometry. *Current Opinion in Chemical Biology* **2022**, *68*, 102132.

(7) Charman, R. J.; Kad, N. M. Single molecule iSCAT imaging reveals a fast, energy efficient search mode for the DNA repair protein UvrA. *Nanoscale* **2022**, *14*, 5174–5184.

(8) Foley, E. D. B.; Kushwah, M. S.; Young, G.; Kukura, P. Mass photometry enables label-free tracking and mass measurement of single proteins on lipid bilayers. *Nature Methods* **2021**, *18*, 1247–1252, Number: 10 Publisher: Nature Publishing Group.

(9) Galvagnion, C.; Buell, A. K.; Meisl, G.; Michaels, T. C. T.; Vendruscolo, M.; Knowles, T. P. J.; Dobson, C. M. Lipid vesicles trigger -synuclein aggregation by stimulating primary nucleation. *Nature Chemical Biology* **2015**, *11*, 229–234, Number: 3 Publisher: Nature Publishing Group.

(10) Hundt, N.; Cole, D.; Hantke, M. F.; Miller, J. J.; Struwe, W. B.; Kukura, P. Direct observation of the molecular mechanism underlying protein polymerization. *Science Advances* **2022**, *8*, Publisher: American Association for the Advancement of Science.

(11) Paul, S. S.; Lyons, A.; Kirchner, R.; Woodside, M. T. Quantifying Oligomer Populations in Real Time during Protein Aggregation Using Single-Molecule Mass Photometry. *ACS Nano* **2022**, *16*, 16462–16470, Publisher: American Chemical Society.

(12) de Wit, G.; Albrecht, D.; Ewers, H.; Kukura, P. Revealing Compartmentalized Diffusion in Living Cells with Interferometric Scattering Microscopy. *Biophysical Journal* **2018**, *114*, 2945–2950.

(13) Young, G. et al. Quantitative mass imaging of single biological macromolecules. *Science* **2018**, *360*, 423–427.

(14) Cole, D.; Young, G.; Weigel, A.; Sebesta, A.; Kukura, P. Label-Free Single-Molecule Imaging with Numerical-Aperture-Shaped Interferometric Scattering Microscopy. *ACS photonics* **2017**, *4*, 211–216.

(15) Wo, X.; Li, Z.; Jiang, Y.; Li, M.; Su, Y.-w.; Wang, W.; Tao, N. Determining the Absolute Concentration of Nanoparticles without Calibration Factor by Visualizing the Dynamic Processes of Interfacial Adsorption. *Analytical Chemistry* **2016**, *88*, 2380–2385.

(16) Melo, L.; Hui, A.; Kowal, M.; Boateng, E.; Poursorkh, Z.; Rocheron, E.; Wong, J.; Christy, A.; Grant, E. Size Distributions of Gold Nanoparticles in Solution Measured by Single-Particle Mass Photometry. *The Journal of Physical Chemistry B* **2021**, *125*, 12466–12475.

(17) Redmon, J.; Divvala, S.; Girshick, R.; Farhadi, A. You Only Look Once: Unified, Real-Time Object Detection. 2016 IEEE Conference on Computer Vision and Pattern Recognition (CVPR). 2016; pp 779–788, ISSN: 1063-6919.

(18) Kashkanova, A. D.; Blessing, M.; Gemeinhardt, A.; Soulat, D.; Sandoghdar, V. Precision size and refractive index analysis of weakly scattering nanoparticles in polydispersions. *Nature Methods* **2022**, *19*, 586–593, Number: 5 Publisher: Nature Publishing Group.

(19) Kukura, P.; Ewers, H.; Müller, C.; Renn, A.; Helenius, A.; Sandoghdar, V. High-speed

nanoscopic tracking of the position and orientation of a single virus. *Nature Methods* **2009**, *6*, 923–927.

(20) Ortega-Arroyo, J.; Kukura, P. Interferometric scattering microscopy (iSCAT): new frontiers in ultrafast and ultrasensitive optical microscopy. *Physical Chemistry Chemical Physics* **2012**, *14*, 15625.

(21) Priest, L.; Peters, J. S.; Kukura, P. Scattering-based light microscopy: from metal nanoparticles to single proteins. *Chemical Reviews* **2021**, *121*, 11937–11970, Publisher: ACS Publications.

(22) Bohren, C. F.; Huffman, D. R. *Absorption and scattering of light by small particles*; John Wiley & Sons, 2008.

(23) Boyd, R. W. Intuitive explanation of the phase anomaly of focused light beams. *Journal of the Optical Society of America* **1980**, *70*, 877.

(24) Mahmoodabadi, R. G.; Taylor, R. W.; Kaller, M.; Spindler, S.; Mazaheri, M.; Kasaian, K.; Sandoghdar, V. Point spread function in interferometric scattering microscopy (iSCAT). Part I: aberrations in defocusing and axial localization. *Optics Express* **2020**, *28*, 25969–25988, Publisher: Optica Publishing Group.

(25) Olsén, E.; Garcia, B.; Skärberg, F.; Parkkila, P.; Volpe, G.; Höök, F.; Midtvedt, D. Dual-angle interferometric scattering microscopy for optical multiparametric particle characterization. *arXiv preprint arXiv:2309.07572* **2023**,

(26) Olsén, E.; Midtvedt, B.; González, A.; Eklund, F.; Ranoszek-Soliwoda, K.; Grobelny, J.; Volpe, G.; Krzyzowska, M.; Höök, F.; Midtvedt, D. Label-free optical quantification of material composition of suspended virus-gold nanoparticle complexes. *arXiv preprint arXiv:2304.07636* **2023**,

(27) Tan, W. K.; Yokoi, A.; Kawamura, G.; Matsuda, A.; Muto, H. PMMA-ITO Composite Formation via Electrostatic Assembly Method for Infra-Red Filtering. *Nanomaterials* **2019**, *9*, 886.

(28) Ortiz-Orruño, U.; Quidant, R.; van Hulst, N. F.; Liebel, M.; Ortega Arroyo, J. Simultaneous Sizing and Refractive Index Analysis of Heterogeneous Nanoparticle Suspensions. *ACS Nano* **2023**, *17*, 221–229, Publisher: American Chemical Society.

(29) Liu, L.; Yellinek, S.; Valdinger, I.; Donval, A.; Mandler, D. Important Implications of the Electrochemical Reduction of ITO. *Electrochimica Acta* **2015**, *176*, 1374–1381.

(30) Ye, H.; Zheng, X.; Yang, H.; Kowal, M.; Seifried, T.; Singh, G. P.; Aayush, K.; Gao, G.; Grant, E.; Kitts, D.; Yada, R.; Yang, T. Rapid Detection of Micro/Nanoplastics Via Integration of Luminescent Metal Phenolic Networks Labeling and Quantitative Fluorescence Imaging in A Portable Device. 2023; `https://chemrxiv.org/engage/chemrxiv/article-details/65161cfa0065940912145855`.

(31) Sundaresan, V.; Monaghan, J. W.; Willets, K. A. Monitoring Simultaneous Electrochemical Reactions with Single Particle Imaging. *ChemElectroChem* **2018**, *5*, 3052–3058.

(32) Xu, S.; Yu, X.; Chen, Z.; Zeng, Y.; Guo, L.; Li, L.; Luo, F.; Wang, J.; Qiu, B.; Lin, Z. Real-Time Visualization of the Single-Nanoparticle Electrocatalytic Hydrogen Generation Process and Activity under Dark Field Microscopy. *Analytical Chemistry* **2020**, *92*, 9016–9023.

(33) Wonner, K.; Evers, M. V.; Tschulik, K. Simultaneous Opto- and Spectro-Electrochemistry: Reactions of Individual Nanoparticles Uncovered by Dark-Field Microscopy. *Journal of the American Chemical Society* **2018**, *140*, 12658–12661.

(34) Lemineur, J.-F.; Noël, J.-M.; Ausserré, D.; Combellas, C.; Kanoufi, F. Combining Electrodeposition and Optical Microscopy for Probing Size-Dependent Single-

Nanoparticle Electrochemistry. *Angewandte Chemie International Edition* **2018**, *57*, 11998–12002.

(35) Dwyer, B.; Nelson, J. .; Solawetz, J.; et. al. Roboflow. 2022; `https://roboflow.com`.

(36) Kowal, M. iSCAT Particle Image Library Dataset. 2023; `https://universe.roboflow.com/iscat-particle-image-library/iscat-particle-image-library`, Publication Title: Roboflow Universe Type: Open Source Dataset Published: https://universe.roboflow.com/iscat-particle-image-library/iscat-particle-image-library.